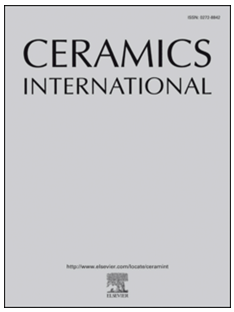

Connecting morphology and photoluminescence emissions in β-Ag_2MoO_4 microcrystals

Vinícius Teodoro, Amanda Fernandes Gouveia, Thales Rafael Machado, Aline Barrios Trench, Natalia Jacomaci, Marcelo Assis, Gilmar Eugenio Marques, Marcio Daldin Teodoro, Miguel Angel San-Miguel, Juan Andrés, Jefferson Bettini, Elson Longo

PII: S0272-8842(21)03298-3

DOI: https://doi.org/10.1016/j.ceramint.2021.10.156

Reference: CERI 30461

To appear in: *Ceramics International*

Received Date: 20 July 2021

Revised Date: 10 October 2021

Accepted Date: 22 October 2021

Please cite this article as: Viní. Teodoro, A.F. Gouveia, T.R. Machado, A.B. Trench, N. Jacomaci, M. Assis, G.E. Marques, M.D. Teodoro, M.A. San-Miguel, J. Andrés, J. Bettini, E. Longo, Connecting morphology and photoluminescence emissions in β-Ag_2MoO_4 microcrystals, *Ceramics International* (2021), doi: https://doi.org/10.1016/j.ceramint.2021.10.156.

Connecting morphology and photoluminescence emissions in β-Ag_2MoO_4 microcrystals

Vinícius Teodoro[1]; Amanda Fernandes Gouveia[2,5]; Thales Rafael Machado[1]; Aline Barrios Trench[1]; Natalia Jacomaci[3]; Marcelo Assis[1]; Gilmar Eugenio Marques[4]; Marcio Daldin Teodoro[4]; Miguel Angel San-Miguel[2]; Juan Andrés[5]; Jefferson Bettini[6]; Elson Longo[1*].

[1]*CDMF, Federal University of São Carlos, P.O. Box 676, São Carlos 13565-905, Brazil*
[2]*Institute of Chemistry, State University of Campinas, 13083-970, Campinas, São Paulo, Brazil*
[3]*Universidade Estadual Paulista, Laboratório Interdisciplinar de Eletroquímica e Cerâmica*
[4]*Department of Physics, Federal University of São Carlos, P.O. Box 676, São Carlos 13565-905, Brazil*
[5]*Department of Analytical and Physical Chemistry, University Jaume I, Castelló 12071, Spain*
[6]*Brazilian Nanotechnology National Laboratory (LNNano)/CNPEM, Campinas, Sao Paulo 13083-970, Brazil*

[*]*Corresponding author*: elson.liec@gmail.com

Abstract

This work elucidates the morphology-photoluminescence (PL) emission relationships, based on experimental and calculated results, on β-Ag_2MoO_4 samples synthesized by microwave-assisted hydrothermal method. It was shown that the solvent (water and ammonia) and temperature (120, 130, 140, and 150°C) play a crucial role in the morphology and PL emissions. A crystal structure model, composed by the local coordination of both Ag and Mo atoms at bulk and exposed surfaces, was built, and the possible mechanism along the synthesis progress was proposed and analyzed. This study provides an idea for the preparation and development of β-Ag_2MoO_4 based materials with desirable properties.

Keywords: β-Ag_2MoO_4, morphology, photoluminescence emissions, DFT calculations.

1. Introduction

Photoluminescence (PL) emission is an important research field that has been investigated and employed for several applications, such as lasers [1], bioimaging [2], gas detection [3], and light-emitting diodes [4]. Among others, the white-light-emitting diode (WLEDs) has attracted attention due to its practical use as backlighting in liquid crystal displays (LCD) [5,6]. Several

methods have been used for obtaining WLEDs, being the combination of blue/green and red colors emitting one of the most employed [7–9]. Therefore, the modification of materials for light-emitting in a given color region is an attractive research field for the further construction of suitable devices.

Among several ways to modify the PL emission of a semiconductor, controlling the morphology is a promising method to modulate the intensity and color region emission [10–13]. The influence of morphology in the PL emission arises from the different exposed surfaces in the nano/micro-particles. Each exposed surface has its atom surface termination, which presents different numbers and kinds of vacancies, such as oxygen vacancies (V_o^x) [14–18]. These defects directly affect the electronic structure of the material and act as recombination centers for electronic transitions, and hence altering the energy and density of photon emission.

Silver molybdate-based materials (β-Ag_2MoO_4) have been investigated for several applications, such as: antibacterial [19], photoluminescent [20], biosensor [21], energy storage [22], and photocatalytic [23]. It has been demonstrated, by both theoretical calculations and experimental evidences, that the β-Ag_2MoO_4 can present several morphologies with different proportions of exposed surfaces, which each possesses different surface terminations [19,24,25]. Herewith, modulating the morphology of β-Ag_2MoO_4 is an interesting way to understand its relationship with PL emission and also to design materials with desirable color region emission for further construction of optical devices.

In this paper, it was reported the solvent and temperature effects on the morphology and PL emissions of β-Ag_2MoO_4 synthetized by the microwave-assisted hydrothermal (MAH) method. The goal is not only to rationalize the experimental results but also to determine the nature of the morphology-dependent PL emissions. As this correlation is quantum mechanical in origin, density functional theory (DFT) calculations were conducted to complement the experimental findings. Therefore, it is presented a well-controlled synthesis of β-Ag_2MoO_4 with different morphologies by using only the MAH method, without any template and/or surfactants. The obtained products were characterized by X-ray diffraction (XRD), Rietveld refinements, Raman spectroscopy, and PL emissions. Field emission scanning electron microscopy (FE-SEM) was employed to observe the crystal morphologies. The results allowed to link the structural to the electronic properties of the exposed surfaces at the morphology, which are difficult or currently impossible to measure. This can potentially streamline the fundamental understanding and rational design of multifunctional materials.

2. Material and methods

The experimental procedure for the synthesis of all samples obtained in water and ammonia, the characterization techniques and computational methods, and the models for β-Ag_2MoO_4 in the DFT calculations are described in detail in the Supporting Information (SI). The samples obtained with water were named according to their corresponding temperatures (120-H, 130-H, 140-H, and 150-H), while those synthetized with ammonia were denominated as 120-N, 130-N, 140-N, and 150-N.

3. Results and discussion

3.1 Structural analysis

The order at long-range of the samples obtained with water and ammonia was analyzed by XRD, and the results are shown in Figure 1a and Figure 1b, respectively. All XRD patterns present sharp and well-defined peaks, suggesting a fine crystallization and structural order at long-range, without any undesirable phase. These results are in good agreement with spinel-type cubic phase of β-Ag_2MoO_4 with $Fd\bar{3}m$ space group and O_h^7 point-group symmetry, according to the Inorganic Crystal Structure Data (ICSD) base No. 28891 [26]. Figure SI-1 shows the full width at half maximum (FWHM) values for the most intense reflection peak (311) for all β-Ag_2MoO_4 samples. As can be seen, for all temperatures employed, the samples obtained with ammonia complexing resulted in higher FWHM values compared to those obtained with only water. The FWHM of an XRD peak can be assigned to the structural order-disorder at long-range, *i.e.*, the periodicity of the unit cell. The use of NH_3 as complexing agent results in the $[Ag(NH_3)_2(H_2O)_6]^+$ complex, instead of $[Ag(H_2O)_6]^+$, formed when water is the solvent. The two strong field NH_3 ligands at the axial axis result in a heterogeneous force field along the $[Ag(NH_3)_2(H_2O)_6]^+$ complex. This fact results in a lower frequency of effective collisions to form the solid related to the homogeneous force field in $[Ag(H_2O)_6]^+$. Therefore, the restricted growth in some directions for the samples obtained with ammonia suppresses the structural organization, resulting in a higher degree of disorder at long-range.

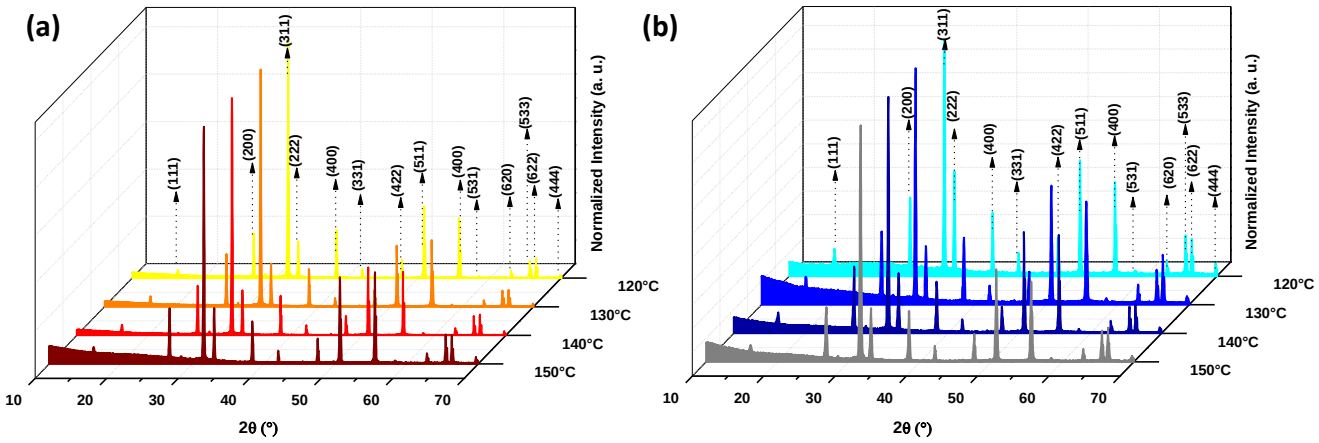

Figure 1 – XRD patterns of β-Ag_2MoO_4 obtained by MAH method in (a) water and (b) ammonia

To identify the crystalline phase and evaluate the structural features of all samples, Rietveld refinements from XRD measurements were performed (see Figure SI-2a-j). The statistical parameters (R_{bragg}, R_{wp}, R_{exp}, and GOF) evaluate the reliability and good quality of the refinements (Table SI-1).

The lattice of β-Ag_2MoO_4 is composed of [AgO_6] and [MoO_4] clusters, which represent the building blocks of this system. The values of Ag−O and Mo−O bond lengths of these clusters and the unit cell volumes are exhibited in Table SI-2. The results indicate that these clusters are symmetric, corresponding to ordered octahedra and tetrahedra, respectively. However, the lengths of Ag−O and Mo−O bonds are longer with respect to the data in ICSD No. 28891 due to an expansion of [AgO_6] and [MoO_4] clusters, resulting in an increase of the lattice parameter (*a*) and the unit cell volume for all obtained samples. Figure 2 shows a representation of the β-Ag_2MoO_4 unit cell with a cubic structure, where the constituent [AgO_6] and [MoO_4] clusters were highlighted. The representation was made in Visualization for Electronic and Structural Analysis (VESTA) software version 3.4 for Windows [27].

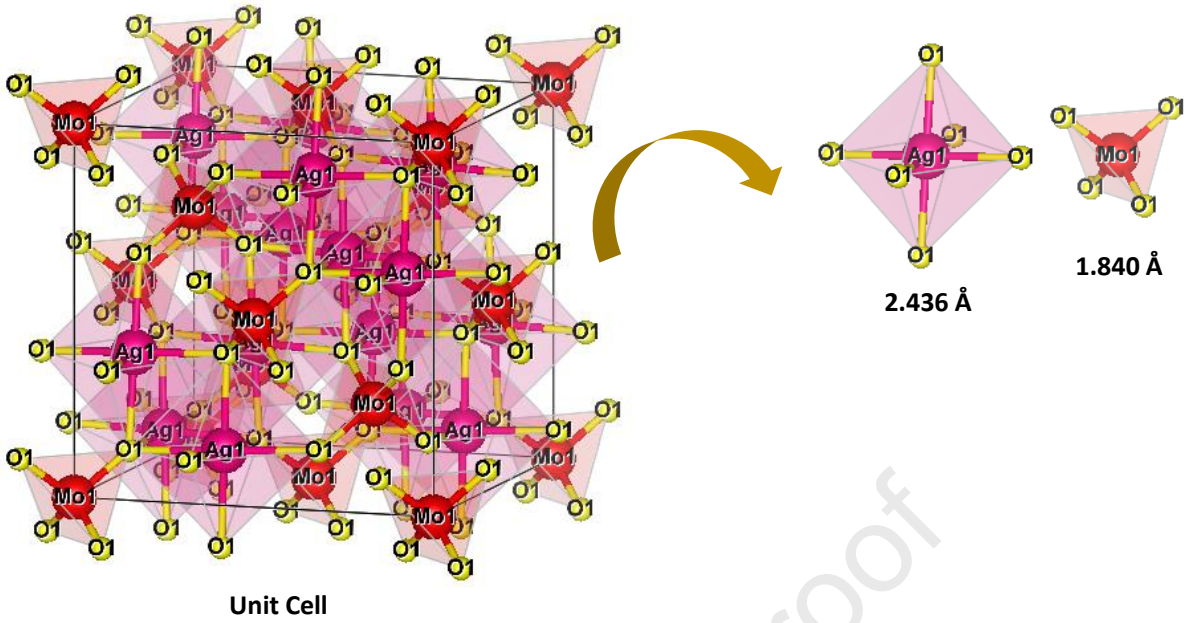

Figure 2 – Unit cell representation of β-Ag_2MoO_4 and the composing [AgO_6] and [MoO_4] clusters

Figure 3a displays the Raman spectra of samples obtained with water. As it can be seen, Raman bands related to the five active modes can be observed. Despite the characteristic low intensity of the Raman band located at approximately 90 cm^{-1}, the bands are sharp and well defined, indicating a good crystallization of the β-Ag_2MoO_4 structure. The Raman active vibrational modes present in β-Ag_2MoO_4 are due to [AgO_6] and [MoO_4] units having specific vibrations within these clusters. The band located at 873 cm^{-1} is associated with the A_{1g} mode, which in turn is related to symmetric stretching of Mo–O bonds within [MoO_4] clusters. The asymmetric stretching of these bonds is responsible for the T_{2g} mode, which is ascribed to the band located at approximately 761 cm^{-1}. The band at around 354 cm^{-1} is attributed to the T_{2g} mode, which in turn is related to bending vibrations of Mo–O bonds in [MoO_4] clusters. The E_g and T_{2g} modes in the bands located at approximately 279 and 90 cm^{-1}, respectively, are ascribed to external vibrations of lattice modes related to Ag^+ cations in [AgO_6] clusters [25,28–30].

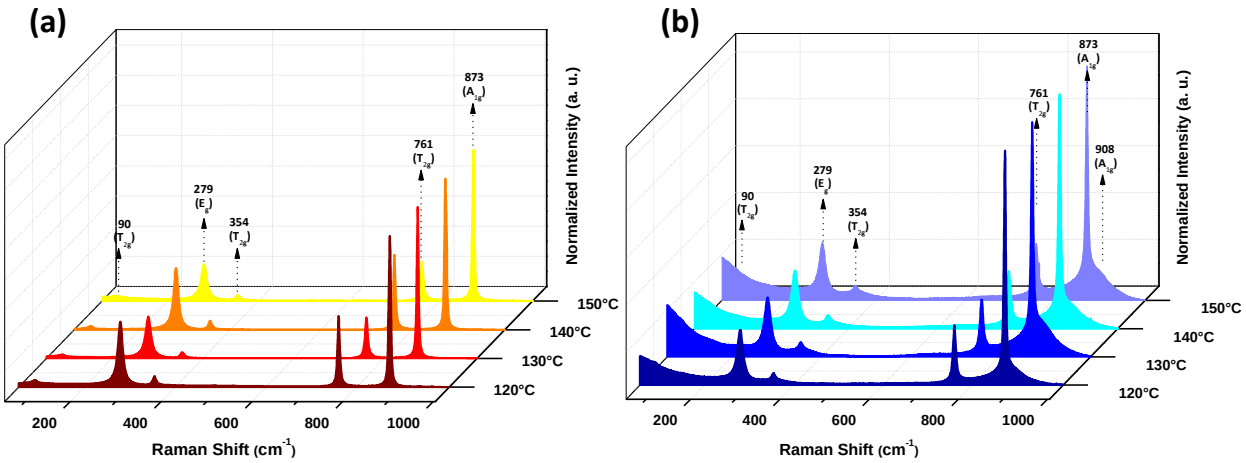

Figure 3 – Raman spectra of β-Ag_2MoO_4 obtained with (a) water and (b) ammonia

Figure 3b shows the Raman spectra of samples obtained with ammonia. The observed Raman bands are sharp and well defined, indicating a good crystallization of these samples in the β-Ag_2MoO_4 structure, like the samples obtained with water. A difference in the Raman spectra for the samples obtained with ammonia in comparison with water can be clearly observed, that is, the appearance of a shoulder in the band located at 873 cm^{-1}. This shoulder at approximately 908 cm^{-1} is also ascribed to the A_{1g} mode due to the widening of the band located at 873 cm^{-1} since this vibrational mode can induce Raman scattering in the range from 872 to 926 cm^{-1} [24]. It was previously observed the emergence of this band extension for β-Ag_2MoO_4 obtained by the co-precipitation method [24]. None of the samples had a significant position shift of Raman bands.

However, variations in FWHM were observed for samples obtained with both water and ammonia. The FWHM values calculated for the band with A_{1g} mode located at 873 cm^{-1} were 6.42, 5.38, 6.40, and 5.46 cm^{-1} for 120-H, 130-H, 140-H, and 150-H samples, respectively. Differently, the calculated values for 120-N, 130-N, 140-N, and 150-N were 5.97, 6.59, 6.60, and 6.92 cm^{-1}, respectively. Therefore, in general, it could be observed that the band at 873 cm^{-1} has a trend to achieve higher values of FWHM for samples obtained with ammonia than with water. Since the A_{1g} mode (873 cm^{-1}) corresponds to the symmetric stretching of Mo−O bonds in [MoO_4] clusters, a widening in its FWHM and the appearance of a shoulder can be related to a broader range of frequencies of this vibrational mode that causes inelastic scattering, *i.e.*, variations in the values of bond lengths provoke changes in the frequencies of the vibrational modes.

3.2 β-Ag_2MoO_4 formation mechanisms

Synthetic routes of solid-state chemistry lack the predictability of the synthesis outcome in comparison with the synthesis methods of organic chemistry, where the molecular units can be linked to form the target product, followed by specific modifications in the functional groups. However, for inorganic solids, the structural analysis becomes more complicated. This is partially because of the lack of efficient real-time methods of structural elucidation for *in situ* formed intermediate solids, making impossible to detect the structure of inorganic solids. Under such circumstances, the natural structural evolution along the synthetic processes, from the adapted reagents/precursors to target products, is usually ambiguous at the atomic scale and represents a challenging task given the diversity of the potential unit structures.

Efforts to develop the corresponding synthetic pathways to the target material comprise the understanding and control of intermolecular interactions in the solid state. In this way, such a structural evolution process in intermediate samples could provide a clear reaction mechanism for a chemical process and would be done by the assembly reaction of building units inside an integrated structure of the defined material. In particular, the solvent effects during the synthesis are often difficult to be understood in cases where reaction intermediates, and consequently their differential behavior in different solvents, are not directly observable by traditional characterization techniques. Here, it was aimed to propose a formation mechanism of β-Ag_2MoO_4.

The crystallization process generally involves a very complex sequence of steps to form 3D structures, including the formation of primary units via dissolution, hydration/dehydration, deamination, nucleation, precipitation, and crystallization. To synthesize β-Ag_2MoO_4 crystals using the MAH method, $Na_2MoO_4{\cdot}2H_2O$, $AgNO_3$, and NH_4OH were used as the starting materials. First, $Na_2MoO_4{\cdot}2H_2O_{(aq)}$ was dissolved to form $(MoO_4)^{2-}{}_{(aq)}$, Eq. SI-2, while $AgNO_3$ was dissolved to generate Ag^+, which in turn forms the $[Ag(H_2O)_6]^+{}_{(aq)}$ complex in aqueous solution, Eq. SI-3. In ammoniacal medium, $NH_4OH_{(aq)}$ reacts with $Ag^+{}_{(aq)}$ to form amineaqua silver (I) complexes, $[Ag(NH_3)_2(H_2O)_4]^+{}_{(aq)}$, Eq. SI-4. This complex is composed of $[Ag(NH_3)_2]^+{}_{(aq)}$, in which two covalent bonds are formed between Ag and N atoms of the NH_3. Besides that, the O atoms of the four water molecules that compose the solvation box interact with the Ag atom by electrostatic forces, rendering the $[Ag(NH_3)_2(H_2O)_4]^+{}_{(aq)}$ complex [31–35]**.** An exchange process involving the H_2O and NH_3 ligands in the first coordination layer between $[Ag(H_2O)_6]^+{}_{(aq)}$ and $[Ag(NH_3)_2(H_2O)_4]^+{}_{(aq)}$, Eq. SI-5, can be proposed, as already demonstrated by molecular simulation studies at an intermediate ratio of NH_3/H_2O [36,37].

The $(MoO_4)^{2-}_{(aq)}$ anion is the precursor of $[MoO_4]$ clusters, while $[Ag(H_2O)_6]^+_{(aq)}$, $[Ag(NH_3)_2(H_2O)_4]^+_{(aq)}$, $[Ag(NH_3)_{2-x}(H_2O)_{4+x}]^+_{(aq)}$ and $[Ag(NH_3)_x(H_2O)_{6-x}]^+_{(aq)}$ cations are the precursors of $[AgO_6]$ clusters, which have different electron density in the complexes, resulting in different morphological aspects, and thus photoluminescence properties. Therefore, during the synthesis, dissolution/dehydration processes take place with concomitant formation of $[AgO_6]$ and $[MoO_4]$ clusters, which act as structural precursors to form the 3D lattice of β-Ag_2MoO_4 in the solid state, Eq. SI-6. According to Gebauer et al. [38], these clusters can be considered structural entities that precede the nucleation, often known as coined pre-nucleation clusters.

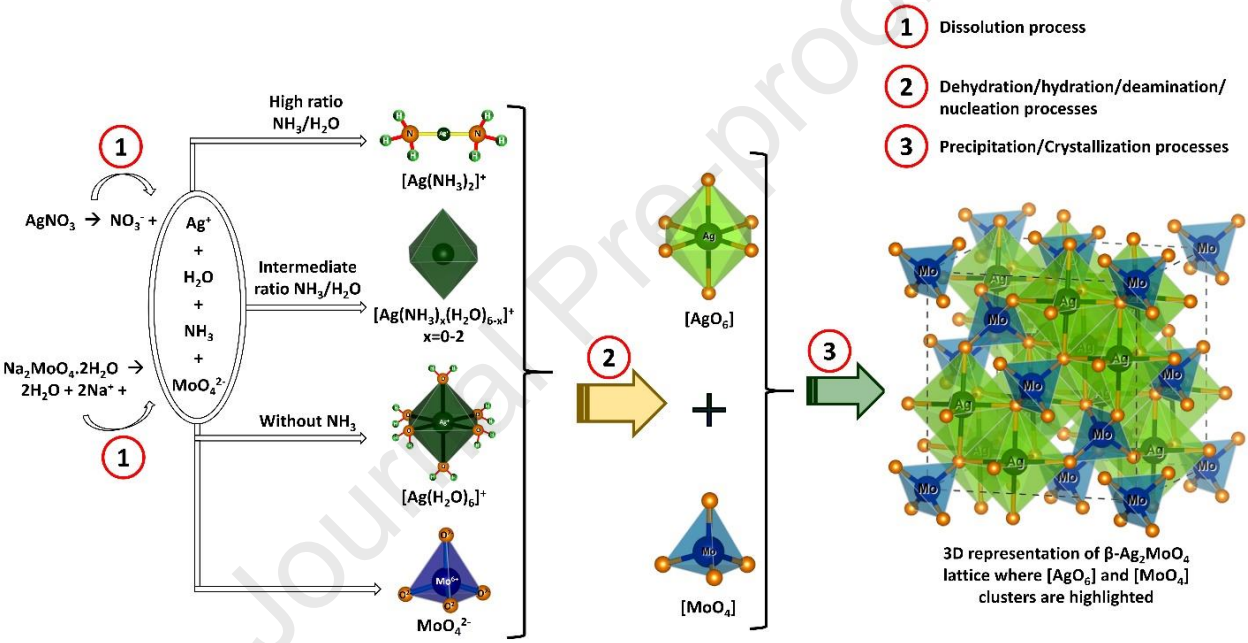

Figure 4 – Pictorial representation of different stages for the formation of the 3D lattice of β-Ag_2MoO_4

A pictorial representation of the process involved in Eq. SI-2-6 is shown in Figure 4. In the classical nucleation theory, the driving force for the nucleation of solids is the decrease of energy, which comprises two steps. The first step is associated with the formation of dense precursors, and the second one corresponds to the nucleation of crystalline nuclei from dense precursors [39,40]. In our case, the first step is the dissolution process (1) that corresponds to a lesser energy barrier step, while the (2) dehydration/deamination/nucleation and (3) crystallization/precipitation processes can be linked to the first and second steps in the classical nucleation theory, respectively.

3.3 Morphological evolution and FE-SEM images

The formation of different morphologies of β-Ag_2MoO_4 samples can be substantiated by FE-SEM investigations. The corresponding FE-SEM images of β-Ag_2MoO_4 samples are presented in Figure 5.

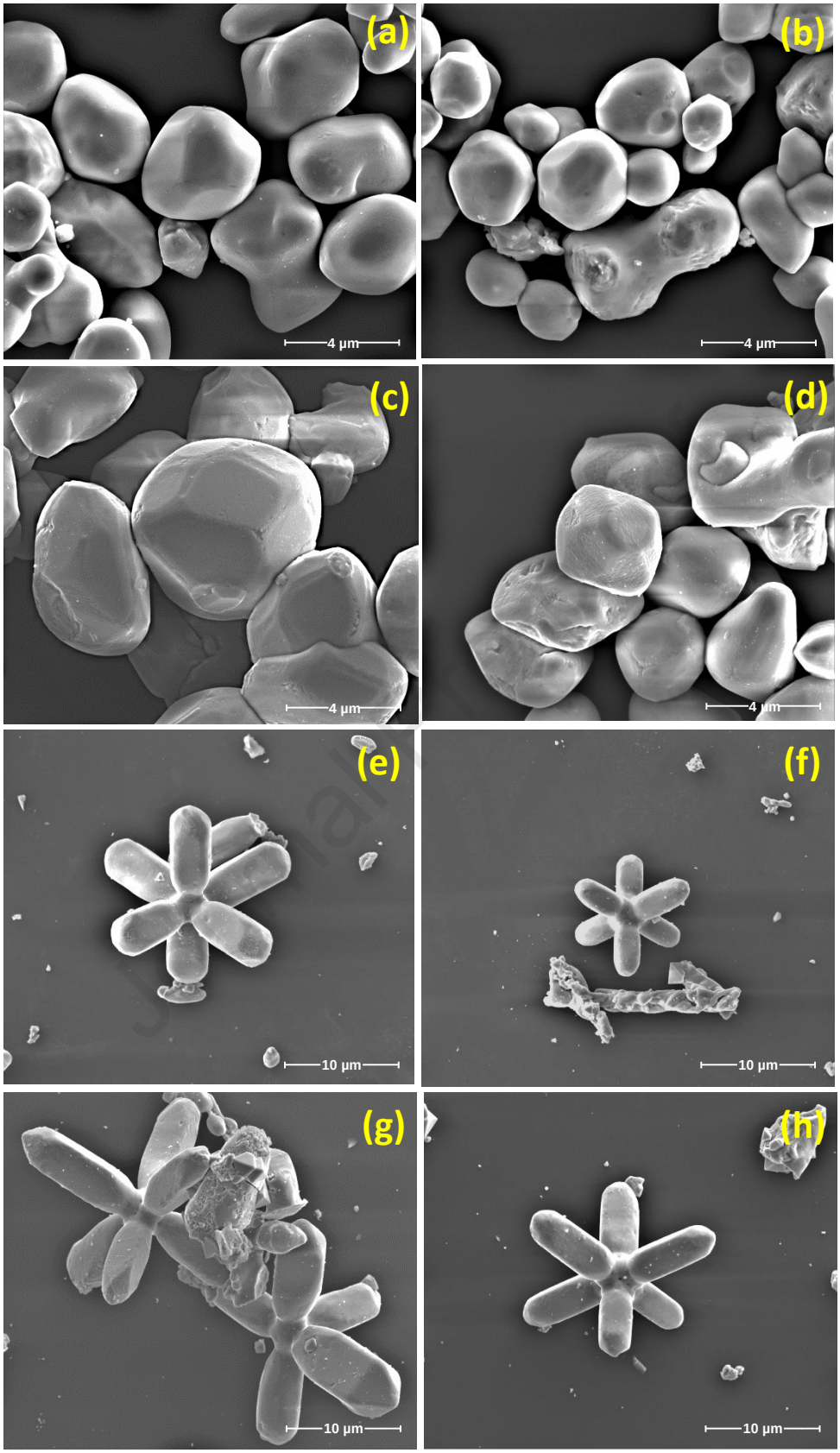

Figure 5 – FE-SEM images for the as-synthetized samples: (a) 120-H, (b) 130-H, (c) 140-H, (d) 150-H, (e) 120-N, (f) 130-N, (g) 140-N, and (h) 150-N

The analysis of the results in Figure 5 indicates that the samples obtained with water as solvent presented microcrystals with quasi-spherical morphologies, as previously reported [41,42]. In contrast, the samples obtained with ammonia as solvent exhibited more defined faceted microcrystals. Through surface delimitation in the microcrystals of the as-synthetized samples, it was possible to see that the corresponding morphologies are in accordance with those predicted by the theoretical Wulff construction.

When the Ag^+ cation is solvated with H_2O, a first homogeneous layer containing six H_2O molecules is formed. Subsequently, random collisions between the $[Ag(H_2O)_6]^+$ complex and the $(MoO_4)^{2-}$ group take place, thus increasing the probability of formation of different surfaces. In other words, when a larger degree of randomness of these processes is reached, the number of available morphologies increases. These morphologies can be assigned to the strong interaction between the local coordination of Ag^+ and $(MoO_4)^{2-}$ ions along with the synthesis progress that leads to a rapid formation of solid nuclei, which grow similarly in all directions. On the other hand, when the Ag^+ is complexed with NH_3, only a fraction of these complexes is able to produce effective collisions with $(MoO_4)^{2-}$ ions due to the strong interaction between Ag^+ and N centers forming the solid nuclei and enabling the subsequent growth process. Therefore, only a few ions have sufficient kinetic energy to overcome the high-energy barrier associated with the rupture of Ag–N in this complex, decreasing the probability of formation of different surfaces and subsequent morphologies. To provide further morphological evidence of the β-Ag_2MoO_4 samples, Figure SI-3 shows other FE-SEM images of all prepared samples.

A detailed analysis of these microcrystals revealed the presence of exposed surfaces at the morphologies derived from theoretical calculations. The use of ammonia in the obtained samples favored the exposure of the (111) surface in their microcrystals. As mentioned above, the weaker interaction between Ag^+ cation and O atoms of H_2O can justify the faster formation of solid nuclei and the subsequent growth processes in the water solvent. In contrast, the stronger interaction between Ag^+ cation and N atoms of NH_3 leads to a lower frequency of effective collisions between these particles, resulting in a lower probability of exposed surfaces in the obtained morphologies. As observed in the micrographs, the samples obtained in ammonia present a six-rod microcrystal with a pyramidal shape on its tip. Moreover, these polyhedral units observed along the sample are agglomerated in the six-rod microcrystals. This is a typical signature of a coalescence process involving these square base bipyramid polyhedral units, in which an isolated unit acts as a center for others to coalesce over each of the six corners of the polyhedron, resulting in a six-rod morphology.

Figure SI-4 shows the particle size distribution and the average particle size (inset) of β-Ag_2MoO_4 samples obtained with water. As it can be seen, the average particle size oscillates as the synthesis temperature increases, reaching values of 4.5, 3.5, 5.8, and 4.3 μm for the samples obtained at 120, 130, 140, and 150°C, respectively. For a better understanding of the formation mechanism of the particles, a comparison between the average particle size of the samples and dispersivity was performed, as shown in Figure 6, where it is possible to note that the oscillations in average particle size have an opposite behavior to the dispersivity values. In other words, the increase in average particle size is followed by a decrease in the sample dispersivity, whereas the decrease in average particle size is followed by a dispersivity increase. This behavior is indicative of the dissolution/precipitation process that determines the crystal growth of the samples obtained with water since the range of particle sizes and the average size varied with the synthesis temperature, demonstrating that this process was continuously occurring.

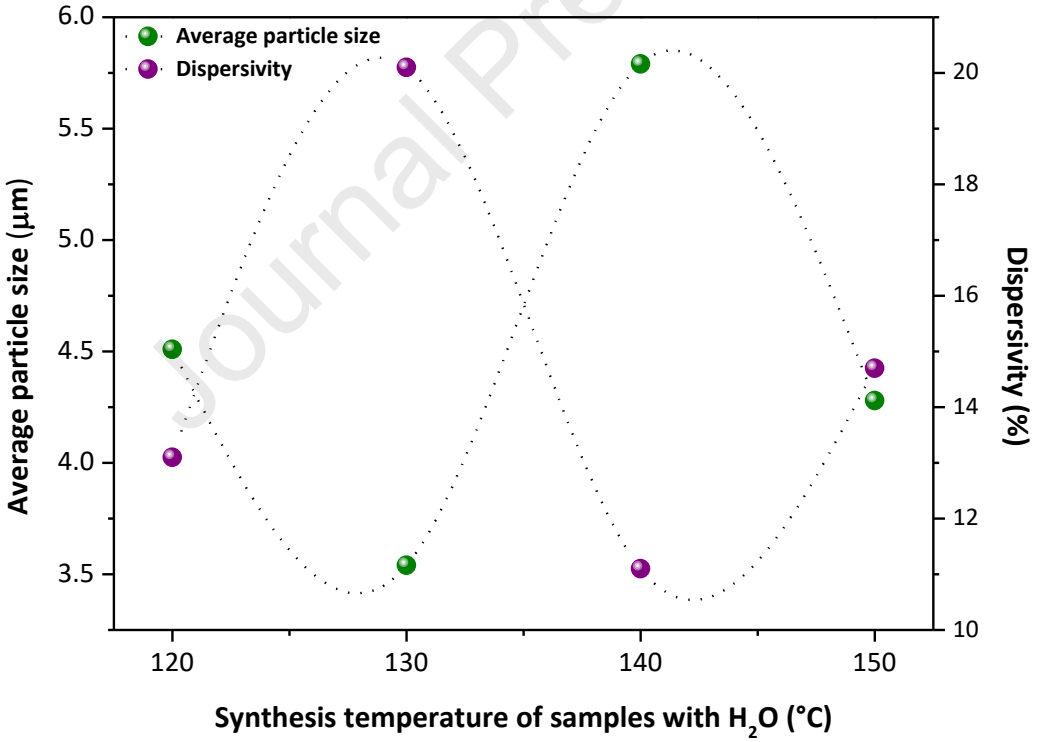

Figure 6 – Average particle size and dispersivity values for samples obtained with water

3.4 Electronic structure of the exposed surfaces and morphologies

The morphology of a crystal is formed by different kinds of facets, and each surface has a determined arrangement of atoms. Figure 7 displays a schematic representation of surface

terminations of the (001), (011), and (111) exposed surfaces obtained by DFT calculations. These undercoordinated clusters are associated with incomplete local coordination of Ag^{+} and Mo^{6+} cations at the exposed surfaces, thus resulting in a lack of Ag−O and Mo−O bonds compared to $[AgO_6]$ and $[MoO_4]$ clusters in the β-Ag_2MoO_4 bulk. The (001) surface presents undercoordinated Ag^{+} and Mo^{6+} cations, suggesting the existence of one and two neutral V_o^x defects, respectively. The (011) surface has two and one V_o^x defects, while the (111) surface presents undercoordinated Ag^{+} cations with the presence of three oxygens. Therefore, it can be concluded that the undercoordinated clusters at the top of each surface are as follows: $[AgO_5]$ and $[MoO_2]$ at the (001) surface, $[AgO_4]$ and $[MoO_3]$ at the (011) surface, and only $[AgO_3]$ at the (111) surface.

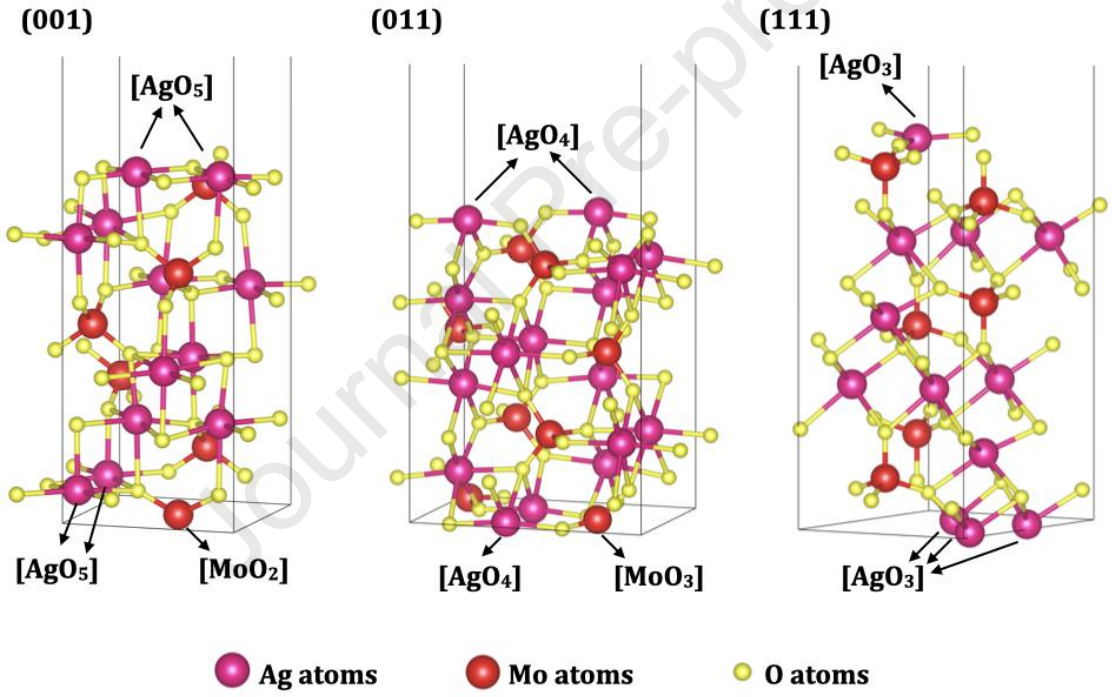

Figure 7 – Surface termination models of (001), (011), and (111) surfaces of β-Ag_2MoO_4

By varying the surface energy values of the (001), (011), and (111) surfaces and employing the Wulff construction, it is possible to obtain the available morphologies of β-Ag_2MoO_4. Figure 8 displays a complete map and the morphologies observed in the FE-SEM images for the samples synthetized with water. Through surface delimitation in the microcrystals of the as-synthetized samples, it was possible to see that the corresponding morphologies are in accordance with those predicted by the theoretical Wulff construction.

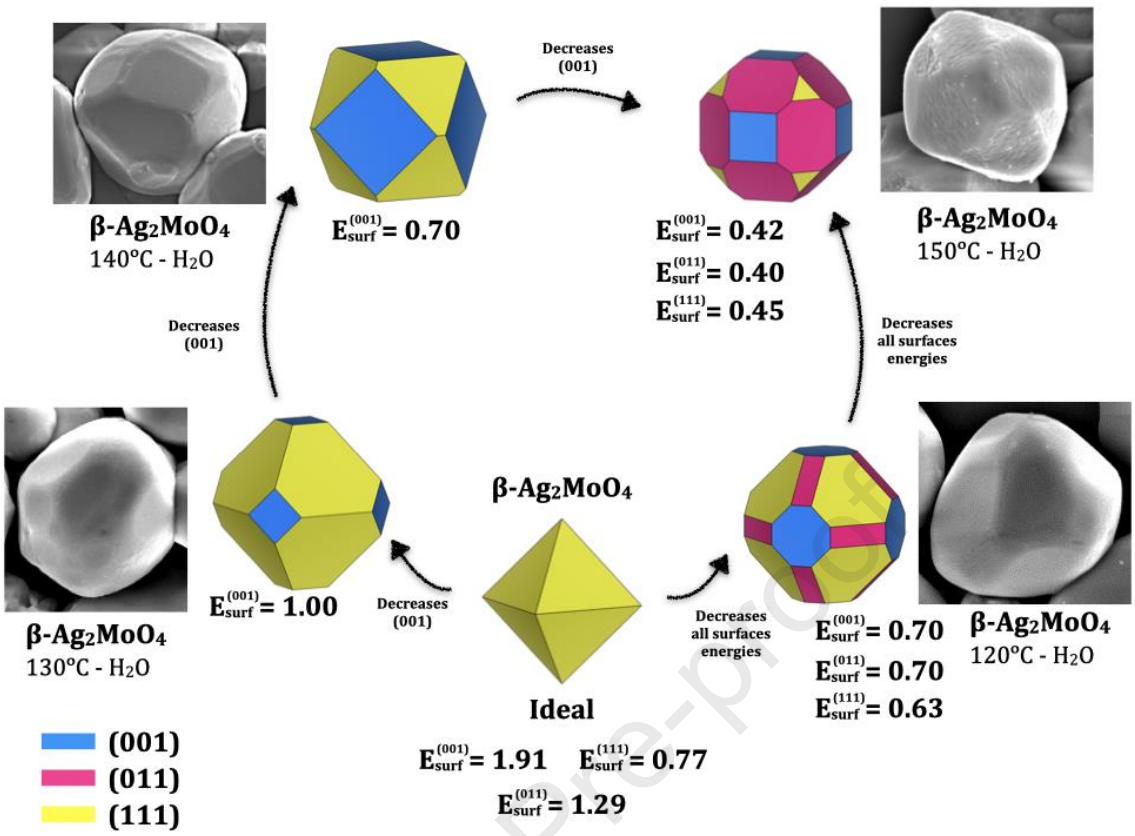

Figure 8 – Calculation of available morphologies of β-Ag_2MoO_4 by using the surface energy values of (001), (011), and (111) surfaces and the Wulff construction. The values of surface energy are in J/m^2. The experimental morphologies can be seen in the inset, where FE-SEM images were inserted for comparison purposes.

The exposed surfaces of the morphologies of the microcrystals synthesized at 120 and 150 °C are composed mainly of (001), (011), and (111) surfaces. However, the contribution of each exposed surface to the final morphology changes. In the samples synthesized at 130 and 140 °C, the (011) surface disappears, being possible to observe only the (001) and (111) surfaces. Despite being very similar, the morphology at 130 °C has a major contribution of the (111) surface, while the morphology at 140 °C has a predominance of the (001) surface.

The ideal β-Ag_2MoO_4 morphology in the center of this map (Figure 8) is different from that previously reported [19,25]. This occurs due to the stability of our (111) surface model and its termination (see Figure 7). In this paper, we found a more stable cut for the (111) surface, with a surface energy value of 0.77 J/m^2 and the presence of an undercoordinated [AgO_3] cluster. Therefore, the ideal morphology is composed of only (111) surfaces.

3.5 PL emissions

Figure 9 displays the PL emissions of the samples obtained by using water and ammonia as solvents. As it can be seen, the PL spectra present a broad band covering the visible spectrum, where all emissions have similar profiles with a minor emission centered in the blue spectral region and a wider band of major emission centered in the red spectral region. The PL emission intensities of samples obtained with ammonia increase with temperature due to the increased structural order-disorder degree [24,43,44], while an opposite behavior can be observed for samples synthetized with water. According to the theoretical calculations, for the samples obtained with ammonia, the increase of the synthesis temperature results in exposed (111) surfaces with a higher proportion of oxygen vacancies. On the other hand, the samples obtained with water present converted exposed (001) and (011) surfaces, comprised of a lower proportion of oxygen vacancies. These oxygen vacancies are responsible for the emission in the red spectral region. Therefore, according to the exposed surface, there is a major emission in the red or blue spectral region, which is influenced by both the temperature and the solvent used in the syntheses. Since these defects directly act as recombination centers, the greater its proportion, the higher the PL emission intensity. Additionally, for temperatures higher than 140 °C, the increment also induces a quenching effect, which in turn induces a slight decrease in PL intensities for both samples due to the order-disorder effects at higher temperatures.

To elucidate the nature and the density of defects responsible for the PL emission, we performed a deconvolution of the overall spectra, in which three main peaks at 443 (blue), 610 (orange), and 703 nm (red) are selected. The blue, orange/green, and red regions of visible spectra are assigned to shallow, intermediate, and deep defects in the semiconductor, and each component content (area percentage) are indicated inside the figure. The PL emission by shallow defects arises from energy states near the conduction and valence bands that are generated by structural distortions. The deep defects are energy states located near the center of the band gap region, which are generated mainly by surface defects such as oxygen vacancies. The intermediate energy states are caused by oxygen vacancies in the bulk structure[45–48].

It is known that surface defects, *i.e.*, oxygen vacancies formed by dangling bonds in the surface [49], are the main responsible for PL emission in the low energy side and in the orange-red spectral region [50–52]. The PL emission in higher energy is widely associated with structural defects, that is, distortions in bond angles within the [MO_x] cluster and also in [MO_x]–[MO_x], being M a given cation [53,54]. It can then be expected that the major

contribution to PL emission of the obtained microcrystals arises from these surface defects with a minor contribution of structural distortions. The samples obtained with ammonia present higher proportions of emission by surface defects, *i.e.*, clusters with oxygen vacancies (undercoordinated), than those obtained with water, besides decreased blue emissions. This increase in orange and red colors can be clearly observed by red shifts in the center of the total band emission, as shown in Figure 9. The PL spectra of the samples obtained with water have an emission band centered at approximately 650 nm, while for samples obtained with ammonia the band center was at approximately 685 nm.

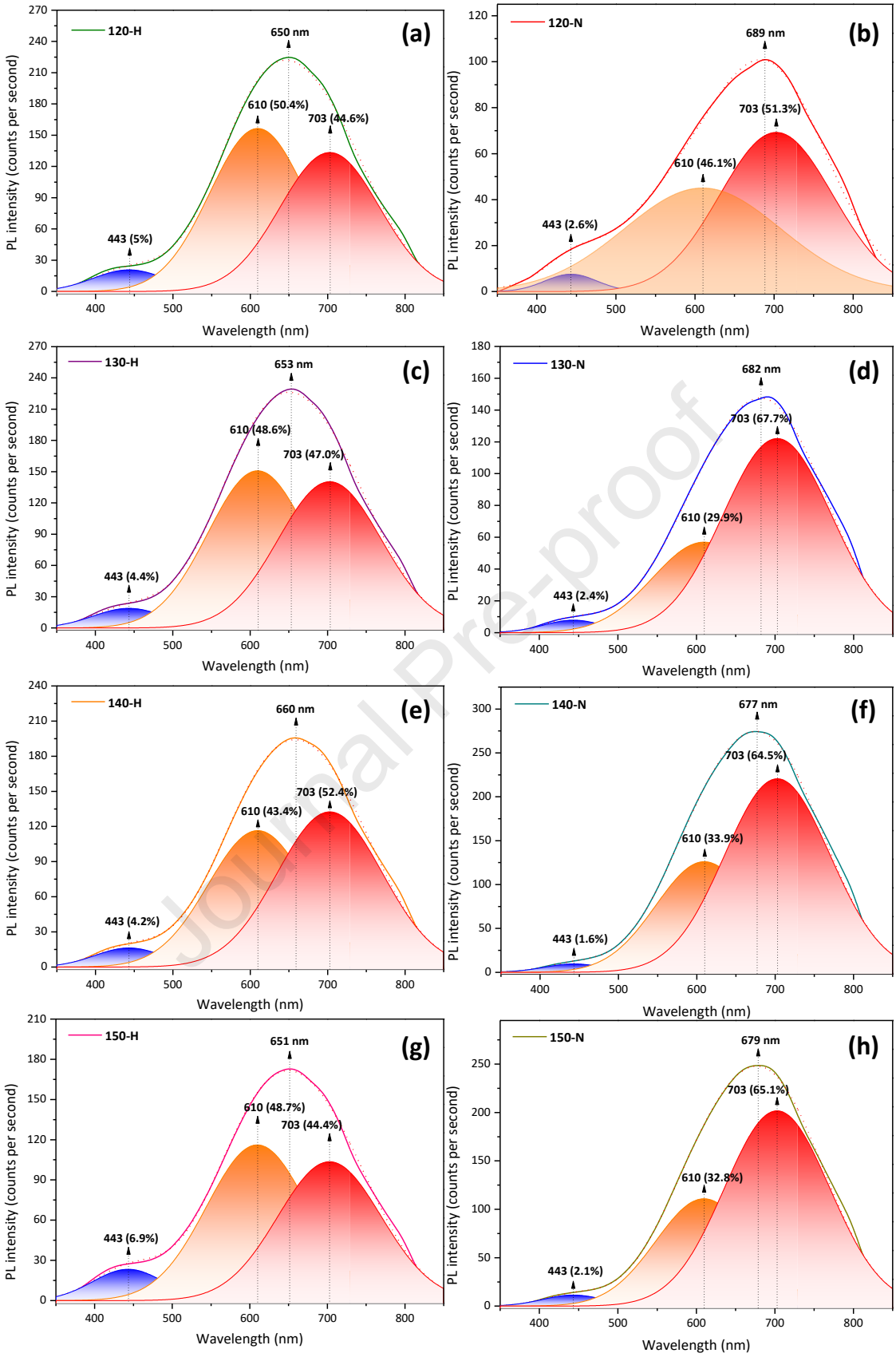

Figure 9 – PL spectra of β-Ag_2MoO_4 samples obtained with water (left panel) and ammonia (right panel. Deconvolution of PL spectra of the samples (a) 120-H, (b) 130-H, (c) 140-H, (d) 150-H, (e) 120-N, (f) 130-N, (g) 140-N and (h) 150-N

The observed morphologies in the samples obtained with water and ammonia have different exposed surfaces in their microcrystals. Each surface has specific defects and a density of defects that are responsible for different properties. As previously seen in FE-SEM images, the samples obtained with water have no defined surfaces in lower temperatures, yet a trend to faceted microcrystals could be observed by increasing the synthesis temperature. As shown in Figure 7, the arrangement of the atoms in the termination of the (001), (011), and (111) surfaces, which were observed in the samples obtained with water at 150 °C, indicates that these surfaces present neutral V_o^x defects in the undercoordinated Ag and Mo clusters. However, the (001) and (011) surfaces have a lower proportion of V_o^x than the (111) surface. As it can be seen in Figure 7, the (001) surface presents four V_o^x per unit cell due to two $[AgO_5 \cdot V_o^x]$ clusters and one $[MoO_2 \cdot 2V_o^x]$ cluster, whereas the (011) surface exhibits five V_o^x per unit cell due to two $[AgO_4 \cdot 2V_o^x]$ clusters and one $[MoO_3 \cdot V_o^x]$ cluster. Meanwhile, the (111) surface termination is the richest in oxygen vacancy, with six V_o^x per unit cell as a result of two $[AgO_3 \cdot 3V_o^x]$ clusters.

Since the use of ammonia in samples obtained by the MAH method favored the exposure of the (111) surface, it can be expected that these samples have high proportions of V_o^x compared to those obtained with water, and consequently higher emission in low energies in the red spectral region, as experimentally observed. The most prominent difference in emission proportions was observed in samples obtained at 150 °C with both water and ammonia, whose values for blue emission were 6.9% and 2.1%, respectively. This difference is a result of the contribution of $[AgO_3 \cdot 3V_o^x]$ clusters to the PL emission of the samples obtained with ammonia. On the contrary, the samples synthetized with water exhibited low proportions of such clusters due to the emergence of $[AgO_4 \cdot 2V_o^x]$, $[MoO_3 \cdot V_o^x]$, $[AgO_5 \cdot V_o^x]$, and $[MoO_2 \cdot 2V_o^x]$ clusters that contribute to the PL emission.

Our theoretical results then confirm that the presence of V_o^x in the surface termination of the morphology due to dangling bonds, which formed undercoordinated clusters, was responsible for the main observed emission exhibited by the microcrystals in energies corresponding to these surface defects, also supporting the difference in emission proportions.

4. Conclusions

Since β-Ag_2MoO_4 has been widely used both in photocatalysis and as bactericide due to its physical and chemical properties, the control of its morphology becomes essential. Morphology and PL emissions are found to change as function of the type of solvent and temperature along the synthesis. Herein, the presented combined experimental and computational approach for the analysis of the different morphologies (quasi-spherical and rod-like) synthetized by the microwave-assisted hydrothermal method with the aid of two solvents, water and ammonia, at temperatures of 120, 130, 140, and 150°C, highlights the most relevant factors (structural and electronic) to tune the PL emissions.

First-principles calculations at the DFT level performed on appropriate surface models of β-Ag_2MoO_4 allowed to gain a deeper understanding of the atomic and electronic structures. The main results of the present study can be summarized as follows: (i) the as-synthesized samples with both solvents exhibited a well-defined spinel-type cubic structure of β-Ag_2MoO_4, as observed by XRD measurements; (ii) the samples obtained with ammonia presented a more structural disorder with a wide range of Mo–O bond distances, indicating a greater presence of oxygen vacancies and a widening of the bands corresponding to the Raman vibrational modes; (iii) the FE-SEM images of the synthesized samples using both water and ammonia as solvents displayed quasi-spherical and rod-like morphologies, respectively, with greater presence of (111) exposed surfaces; (iv) based on the Wulff construction, our DFT calculations showed that the (111) surface is the most stable one as a result of its lower surface energy, in contrast to the particles obtained with water, which presented additional (001) and (011) exposed surfaces; (v) compared the samples synthetized with water, the PL emissions of the samples obtained with ammonia presented a red shift with broadband emission in the red region, which is characteristic of the presence of oxygen vacancies at the exposed surface; and (vi) our theoretical calculations demonstrated that the (111) surface has a large number of oxygen vacancies and is composed of two $[AgO_3 \cdot 3V_o^x]$ clusters, which are responsible for the PL red emission of the samples obtained with ammonia.

The theoretical calculations, together with the experimental results, provide critical clues to understand the nature of the morphology-PL relationship for the modulation of color-selective emitting β-Ag_2MoO_4-based materials. It is also worth noting that the concepts and procedures employed in this work can be applied for synthesis with controlled morphology and photoluminescence emissions of other materials.

Acknowledgements

The authors acknowledge the financial support of the Brazilian agencies: Fundação de Amparo à Pesquisa do Estado de São Paulo (FAPESP, 2013/07296-2; 2016/23891-6; 2017/26105-4, 2019/01732-1), Conselho Nacional de Desenvolvimento Científico e Tecnológico (CNPq, 142035/2017-3, 305792/2020-2), and Coordenação de Aperfeiçoamento de Pessoal de Nível Superior - Brasil (CAPES) - Finance Code 001, and. J.A. acknowledges the financial support from Ministerio de Ciencia, Innovación y Universidades (Spain) project PGC2018-094417-B-I00, and Universitat Jaume I, project no. UJI-B2019-30. A.F.G acknowledges the Universitat Jaume I for the postdoctoral contract (POSDOC/2019/30). This work used computational resources from Centro Nacional de Processamento de Alto Desempenho em São Paulo (CENAPAD-SP) and Centro de Computação John David Rogers (CCJDR-UNICAMP).

References

[1] Y. Wang, Y. Lian, Y. Zhang, C. Tu, D. Xue, A series of Er^{3+}-activated $SrLaGa_3O_7$ single crystal fibers for mid-infrared laser application, J. Rare Earths. 38 (2020) 523–530. doi:10.1016/j.jre.2019.12.014.

[2] Q. Xin, H. Shah, W. Xie, Y. Wang, X. Jia, A. Nawaz, M. Song, J.R. Gong, Preparation of blue- and green-emissive nitrogen-doped graphene quantum dots from graphite and their application in bioimaging, Mater. Sci. Eng. C. 119 (2021) 111642. doi:10.1016/j.msec.2020.111642.

[3] I. Yanase, K. Hayashizaki, M. Kakiage, H. Takeda, Novel application of Tb-substituted layered double hydroxides to capturing and photoluminescence detecting CO_2 gas at ambient temperature, Inorg. Chem. Commun. 125 (2021) 108394. doi:10.1016/j.inoche.2020.108394.

[4] D. Wu, J. Zhou, X. Lin, J. Lin, L. Shi, J. Ding, Q. Wu, Structure, Luminescence, and Energy Transfer of a Narrow-Band Green-Emitting Phosphor $Ce_5Si_3O_{12}N:Tb^{3+}$ for Near-Ultraviolet Light-Emitting Diode-Driven Liquid-Crystal Display, ACS Appl. Electron. Mater. 3 (2021) 406–414. doi:10.1021/acsaelm.0c00948.

[5] H. Liao, M. Zhao, Y. Zhou, M.S. Molokeev, Q. Liu, Q. Zhang, Z. Xia, Polyhedron Transformation toward Stable Narrow-Band Green Phosphors for Wide-Color-Gamut Liquid Crystal Display, Adv. Funct. Mater. 29 (2019) 1901988. doi:10.1002/adfm.201901988.

[6] M. Li, J. Zhou, G. Zhou, M.S. Molokeev, J. Zhao, V. Morad, M. V. Kovalenko, Z. Xia, Hybrid Metal Halides with Multiple Photoluminescence Centers, Angew. Chemie - Int. Ed. 58 (2019) 18670–18675. doi:10.1002/anie.201911419.

[7] A. Yang, B. Yao, Z. Ding, R. Deng, Y. Li, N–$SrTiO_3$/p-GaN heterojunctions: A white light-emitting diode with a broad luminescence spectrum, Mater. Sci. Semicond. Process. 126 (2021) 105659. doi:10.1016/j.mssp.2021.105659.

[8] Y. Xu, T. Chen, Z. Xie, W. Jiang, L. Wang, W. Jiang, X. Zhang, Highly efficient Cu-In-Zn-S/ZnS/PVP composites based white light-emitting diodes by surface modulation, Chem. Eng. J. 403 (2021) 126372. doi:10.1016/j.cej.2020.126372.

[9] M. Zhang, Y. Li, K. Du, X. Gao, Y. Lu, D. Wen, S. Yao, J. Feng, H. Zhang, One-step conversion of $CsPbBr_3$ into $Cs_4PbBr_6/CsPbBr_3@Ta_2O_5$ core-shell microcrystals with enhanced stability and photoluminescence, J. Mater. Chem. C. 9 (2021) 1228–1234.

doi:10.1039/d0tc05039c.

[10] T.K. Le, M. Kang, S.W. Kim, Morphology engineering, room-temperature photoluminescence behavior, and sunlight photocatalytic activity of V_2O_5 nanostructures, Mater. Charact. 153 (2019) 52–59. doi:10.1016/j.matchar.2019.04.046.

[11] O. Marin, V. González, M. Tirado, D. Comedi, Effects of methanol on morphology and photoluminescence in solvothermal grown ZnO powders and ZnO on Si, Mater. Lett. 251 (2019) 41–44. doi:10.1016/j.matlet.2019.05.033.

[12] N. Dirany, A. Hallaoui, J.C. Valmalette, M. Arab, Effect of morphology and temperature treatment control on the photocatalytic and photoluminescence properties of $SrWO_4$ crystals, Photochem. Photobiol. Sci. 19 (2020) 235–250. doi:10.1039/c9pp00331b.

[13] Z. Lin, Q. Zhu, Y. Dong, S. Liu, J.G. Li, X. Li, D. Huo, M. Zhang, M. Xie, X. Sun, Synthesis and formation mechanisms of morphology-controllable indium-containing precursors and optical properties of the derived In_2O_3 particles, CrystEngComm. 18 (2016) 3768–3776. doi:10.1039/c6ce00115g.

[14] M. Assis, C.C. de Foggi, V. Teodoro, J.P. de C. da Costa, C.E. Silva, T. Robeldo, P.F. Caperucci, C.E. Vergani, R.C. Borra, I. Sorribes, A.F. Gouveia, M.A. San-Miguel, J. Andrés, E. Longo, Surface-dependent photocatalytic and biological activities of Ag_2CrO_4: Integration of experiment and simulation, Appl. Surf. Sci. 545 (2021) 148964. doi:10.1016/j.apsusc.2021.148964.

[15] A.C.M. Tello, M. Assis, R. Menasce, A.F. Gouveia, V. Teodoro, G.E. Marques, M.D. Teodoro, N. Jacomaci, M.A. Zaghete, J. Andre, B.F. Silva, E. Longo, Microwave-Driven Hexagonal-to-Monoclinic Transition in $BiPO_4$: An In-Depth Experimental Investigation and First-Principles Study, Inorg. Chem. 59 (2020) 7453–7468. doi:10.1021/acs.inorgchem.0c00181.

[16] P.F.S. Pereira, A.F. Gouveia, M. Assis, R.C. De Oliveira, I.M. Pinatti, M. Penha, L. Gracia, J. Andre, E. Longo, $ZnWO_4$ nanocrystals: synthesis, morphology, photoluminescence and photocatalytic properties, Phys. Chem. Chem. Phys. 20 (2018) 1923–1937. doi:10.1039/c7cp07354b.

[17] I.M. Pinatti, A.B. Trench, A.C.M. Tello, P.F.S. Pereira, J.C. Souza, M.D. Teodoro, I.L. V. Rosa, J. Andrés, E. Longo, A.Z. Simões, Structure, Photoluminescence Emissions, and Photocatalytic Activity of Ag_2SeO_3: A Joint Experimental and Theoretical Investigation, Inorg. Chem. 60 (2021) 5937–5954. doi:10.1021/acs.inorgchem.1c00368.

[18] A.F. Gouveia, L. Gracia, E. Longo, M.A. San-Miguel, J. Andrés, Modulating the properties of multifunctional semiconductors by means of morphology: Theory meets experiments, Comput. Mater. Sci. 188 (2021) 110217. doi:10.1016/j.commatsci.2020.110217.

[19] C.C. De Foggi, R.C. de Oliveira, M. Assis, M.T. Fabbro, V.R. Mastelaro, C.E. Vergani, L. Gracia, J. Andrés, E. Longo, A.L. Machado, Unvealing the role of β-Ag_2MoO_4 microcrystals to the improvement of antibacterial activity, Mater. Sci. Eng. C. 111 (2020) 110765. doi:10.1016/j.neubiorev.2019.07.019.

[20] P.B. Almeida, I.M. Pinatti, R.C. de Oliveira, M.M. Teixeira, C.C. Santos, T.R. Machado, E. Longo, I.L.V. Rosa, Structural, morphological and photoluminescence properties of β-Ag_2MoO_4 doped with Eu^{3+}, Chem. Pap. 75 (2021) 1869–1882. doi:10.1007/s11696-020-01489-4.

[21] N. Pachauri, G.B.V.S. Lakshmi, S. Sri, P.K. Gupta, P.R. Solanki, Silver molybdate nanoparticles based immunosensor for the non-invasive detection of Interleukin-8 biomarker, Mater. Sci. Eng. C. 113 (2020) 110911. doi:10.1016/j.msec.2020.110911.

[22] A. Zareie-Darmian, H. Farsi, A. Farrokhi, R. Sarhaddi, Z. Li, Elucidating the electronic structures of β-Ag_2MoO_4 and Ag_2O nanocrystals via theoretical and experimental approaches towards electrochemical water splitting and CO_2 reduction, Phys. Chem.

Chem. Phys. 23 (2021) 9539–9552. doi:10.1039/d0cp05673a.
[23] G.S. Sousa, F.X. Nobre, E.A.A. Júnior, R.D.S. Bezerra, M.E. De Matos, M.R.M.C. Santos, Photocatalytic performance of β-Ag_2MoO_4 microcrystals at different experimental conditions, Environ. Nanotechnology, Monit. Manag. 14 (2020) 100379. doi:10.1016/j.enmm.2020.100379.
[24] M.T. Fabbro, C.C. Foggi, L.P.S. Santos, L. Gracia, A. Perrin, C. Perrin, C.E. Vergani, A.L. Machado, J. Andrés, E. Cordoncillo, E. Longo, Synthesis, antifungal evaluation and optical properties of silver molybdate microcrystals in different solvents: a combined experimental and theoretical study, Dalt. Trans. 45 (2016) 10736–10743. doi:10.1039/C6DT00343E.
[25] M.T. Fabbro, C. Saliby, L.R. Rios, F.A. La Porta, L. Gracia, M.S. Li, J. Andrés, L.P.S. Santos, E. Longo, Identifying and rationalizing the morphological, structural, and optical properties of β-Ag_2MoO_4 microcrystals, and the formation process of Ag nanoparticles on their surfaces: combining experimental data and first-principles calculations, Sci. Technol. Adv. Mater. 16 (2015) 065002. doi:10.1088/1468-6996/16/6/065002.
[26] J. Donohue, W. Shand, The Determination of the Interatomic Distances in Silver Molybdate, Ag_2MoO_4, J. Am. Chem. Soc. 69 (1947) 222–223. doi:10.1021/ja01194a010.
[27] K. Momma, F. Izumi, VESTA 3 for three-dimensional visualization of crystal, volumetric and morphology data, J. Appl. Crystallogr. 44 (2011) 1272–1276. doi:10.1107/S0021889811038970.
[28] A. Beltrán, L. Gracia, E. Longo, J. Andrés, First-Principles Study of Pressure-Induced Phase Transitions and Electronic Properties of Ag_2MoO_4, J. Phys. Chem. C. 118 (2014) 3724–3732. doi:10.1021/jp4118024.
[29] J.V.B. Moura, T.S. Freitas, R.P. Cruz, R.L.S. Pereira, A.R.P. Silva, A.T.L. Santos, J.H. da Silva, C. Luz-Lima, P.T.C. Freire, H.D.M. Coutinho, β-Ag_2MoO_4 microcrystals: Characterization, antibacterial properties and modulation analysis of antibiotic activity, Biomed. Pharmacother. 86 (2017) 242–247. doi:10.1016/j.biopha.2016.12.016.
[30] J. Andrés, M.M. Ferrer, L. Gracia, A. Beltran, V.M. Longo, G.H. Cruvinel, R.L. Tranquilin, E. Longo, A Combined experimental and theoretical study on the formation of Ag filaments on β-Ag_2MoO_4 induced by electron irradiation, Part. Part. Syst. Charact. 32 (2015) 646–651. doi:10.1002/ppsc.201400162.
[31] P. Woidy, F. Kraus, The Diammine Silver(I) Acetate $[Ag(NH_3)_2]OAc$, Z. Anorg. Allg. Chem. 639 (2013) 2643–2647. doi:10.1002/zaac.201300338.
[32] M. Montazer, A. Shamei, F. Alimohammadi, Synthesis of nanosilver on polyamide fabric using silver/ammonia complex, Mater. Sci. Eng. C. 38 (2014) 170–176. doi:10.1016/j.msec.2014.01.044.
[33] J. Dentzer, P. Ehrburger, J. Lahaye, Adsorption and decomposition of silver diammine complexes on carbon surfaces, J. Colloid Interface Sci. 112 (1986) 170–177. doi:10.1016/0021-9797(86)90079-2.
[34] K.B. Nilsson, I. Persson, V.G. Kessler, Coordination chemistry of the solvated Ag^I and Au^I ions in liquid and aqueous ammonia, trialkyl and triphenyl phosphite, and tri-n-butylphosphine solutions, Inorg. Chem. 45 (2006) 6912–6921. doi:10.1021/ic060175v.
[35] V. Stert, L. Hesse, C.P. Schulz, W. Radloff, Photoinduced ultrafast dynamics in $Ag(NH_3)_n$ clusters, Chem. Phys. Lett. 341 (2001) 501–506. doi:10.1016/S0009-2614(01)00533-4.
[36] S. Sansotta, D. Zahn, Solvation structure and dynamics of Ag^+ in aqueous ammonia solutions: A molecular simulation study, J. Chem. Phys. 147 (2017) 114506. doi:10.1063/1.5003654.

[37] T. Shoeib, R.K. Milburn, G.K. Koyanagi, V. V. Lavrov, D.K. Bohme, K.W.M. Siu, A.C. Hopkinson, A study of complexes $Mg(NH_3)_n^+\cdot$ and $Ag(NH_3)_n^+$, where n = 1-8: Competition between direct coordination and solvation through hydrogen bonding, Int. J. Mass Spectrom. 201 (2000) 87–100. doi:10.1016/S1387-3806(00)00213-X.

[38] D. Gebauer, M. Kellermeier, J.D. Gale, L. Bergström, H. Cölfen, Pre-nucleation clusters as solute precursors in crystallisation, Chem. Soc. Rev. 43 (2014) 2348–2371. doi:10.1039/c3cs60451a.

[39] G.C. Sosso, J. Chen, S.J. Cox, M. Fitzner, P. Pedevilla, A. Zen, A. Michaelides, Crystal Nucleation in Liquids: Open Questions and Future Challenges in Molecular Dynamics Simulations, Chem. Rev. 116 (2016) 7078–7116. doi:10.1021/acs.chemrev.5b00744.

[40] D. Erdemir, A.Y. Lee, A.S. Myerson, Nucleation of crystals from solution: Classical and two-step models, Acc. Chem. Res. 42 (2009) 621–629. doi:10.1021/ar800217x.

[41] F.S. Cunha, J.C. Sczancoski, I.C. Nogueira, V.G. de Oliveira, S.M.C. Lustosa, E. Longo, L.S. Cavalcante, Structural, morphological and optical investigation of β-Ag_2MoO_4 microcrystals obtained with different polar solvents, CrystEngComm. 17 (2015) 8207–8211. doi:10.1039/C5CE01662B.

[42] J.V. Kumar, R. Karthik, S.M. Chen, V. Muthuraj, C. Karuppiah, Fabrication of potato-like silver molybdate microstructures for photocatalytic degradation of chronic toxicity ciprofloxacin and highly selective electrochemical detection of H_2O_2, Sci. Rep. 6 (2016) 34149–34161. doi:10.1038/srep34149.

[43] M. Anicete-Santos, E. Orhan, M.A.M.A. De Maurera, L.G.P. Simões, A.G. Souza, P.S. Pizani, E.R. Leite, J.A. Varela, J. Andrés, A. Beltrán, E. Longo, Contribution of structural order-disorder to the green photoluminescence of $PbWO_4$, Phys. Rev. B. 75 (2007) 165105. doi:10.1103/PhysRevB.75.165105.

[44] S. De Lazaro, J. Milanez, A.T. De Figueiredo, V.M. Longo, V.R. Mastelaro, F.S. De Vicente, A.C. Hernandes, J.A. Varela, E. Longo, Relation between photoluminescence emission and local order-disorder in the $CaTiO_3$ lattice modifier, Appl. Phys. Lett. 90 (2007) 111904. doi:10.1063/1.2713359.

[45] C. Spindler, T. Galvani, L. Wirtz, G. Rey, S. Siebentritt, Excitation-intensity dependence of shallow and deep-level photoluminescence transitions in semiconductors, J. Appl. Phys. 126 (2019) 175703. doi:10.1063/1.5095235.

[46] I.M. Iani, V. Teodoro, N.L. Marana, U. Coleto, J.R. Sambrano, A.Z. Simões, M.D. Teodoro, E. Longo, L.A. Perazolli, R.A.C. Amoresi, M.A. Zaghete, Cation-exchange mediated synthesis of hydrogen and sodium titanates heterojunction: Theoretical and experimental insights toward photocatalyic mechanism, Appl. Surf. Sci. 538 (2021) 148137. doi:10.1016/j.apsusc.2020.148137.

[47] G.S. Silva, L. Gracia, M.T. Fabbro, L.P. Serejo dos Santos, H. Beltrán-Mir, E. Cordoncillo, E. Longo, J. Andrés, Theoretical and experimental insight on Ag_2CrO_4 microcrystals: synthesis, characterization, and photoluminescence properties, Inorg. Chem. 55 (2016) 8961–8970. doi:10.1021/acs.inorgchem.6b01452.

[48] T.R. Machado, J.C. Sczancoski, H. Beltrán-Mir, M.S. Li, J. Andrés, E. Cordoncillo, E. Leite, E. Longo, Structural properties and self-activated photoluminescence emissions in hydroxyapatite with distinct particle shapes, Ceram. Int. 44 (2018) 236–245. doi:10.1016/j.ceramint.2017.09.164.

[49] H. Yoo, M. Kim, C. Bae, S. Lee, H. Kim, T.K. Ahn, H. Shin, Understanding photoluminescence of monodispersed crystalline anatase TiO_2 nanotube arrays, J. Phys. Chem. C. 118 (2014) 9726–9732. doi:10.1021/jp4125588.

[50] E. Silva Junior, F.A. La Porta, M.S. Liu, J. Andrés, J.A. Varela, E. Longo, A relationship between structural and electronic order–disorder effects and optical properties in crystalline TiO_2 nanomaterials, Dalt. Trans. 44 (2015) 3159–3175.

doi:10.1039/c4dt03254c.

[51] C.C. Mercado, F.J. Knorr, J.L. Mchale, S.M. Usmani, A.S. Ichimura, L. V Saraf, Location of Hole and Electron Traps on Nanocrystalline Anatase TiO_2, J. Phys. Chem. C. 116 (2012) 10796−10804.

[52] F.J. Knorr, J.L. McHale, Spectroelectrochemical Photoluminescence of Trap States of Nanocrystalline TiO_2 in Aqueous Media, J. Phys. Chem. C. 117 (2013) 13654–13662. doi:10.1021/jp402264p.

[53] G.F. Teixeira, E. Silva Junior, A.Z. Simões, E. Longo, M.A. Zaghete, Unveiling the correlation between structural order-disorder character and photoluminescence emissions of $NaNbO_3$, CrystEngComm. 19 (2017) 4378–4392. doi:10.1039/c7ce00218a.

[54] T.M. Mazzo, L.R. Macario, L.F. Gorup, V. Bouquet, S. Députier, S. Ollivier, M. Guilloux-Viry, A.R. Albuquerque, J.R. Sambrano, F.A. La Porta, E. Longo, Controlling the Electronic, Structural, and Optical Properties of Novel $MgTiO_3/LaNiO_3$ Nanostructured Films for Enhanced Optoelectronic Devices, ACS Appl. Nano Mater. 2 (2019) 2612–2620. doi:10.1021/acsanm.8b02110.

Declaration of interests

☒ The authors declare that they have no known competing financial interests or personal relationships that could have appeared to influence the work reported in this paper.

☐The authors declare the following financial interests/personal relationships which may be considered as potential competing interests: